Interaction between incident and reflected mechanical waves in the presence of an opposing wind

Fabio Addona

University of Parma, Department of Engineering and Architecture, Parma, 43124, Italy

ARTICLE INFO

ABSTRACT

The interaction between wind and waves largely determines exchanges of mass, momentum, energy, and substances which take place at the air–sea interface. Usually, the parameterization of such interaction considers only the case of progressive waves. However, reflection is practically ubiquitous in the field, especially in coastal areas, and in the lab. Recent experimental studies have extensively treated this subject, showing that even a small amount of wave reflection can significantly modify the free surface elevation and the velocity field on the water side. Nonetheless, a theoretical framework for an exhaustive description of the wave reflection role is still lacking. In this work, an analytical model is developed to emphasize the role of reflection in terms of incident-reflected waves interaction in the 2D momentum equations. A non-null interaction between the incident and the reflected waves is predicted for partially-reflected monochromatic waves, and it is represented by a reflection-induced stress tensor. A phase shift is found among the total wave height, the velocity and the shear stress, with implications on the partition of the wave velocity and stresses. Then, the incident, reflected, and total components of the velocity and of the stresses along the regular wave phase are compared with a set of laboratory experiments, where monochromatic waves in condition of partial reflection are ruffled by an opposing wind. The overlap between experiments and theory is remarkably good, thus validating the entire procedure and assumptions. From the experiments, the fluctuating shear stress and kinetic energy are also extracted for different reflection conditions of the mechanical wave, showing a peak of both quantities near the wave trough (close to the surface). Overall, the experimental analysis gives insights into the velocity, momentum and energy fluxes along the wave phase, based on velocity measurements at one fetch length.

1. Introduction

It is common to observe waves propagating at the ocean surface, often ruffled by winds and travelling over underlying currents (Sullivan and McWilliams, 2010). The overall conditions at the air–sea interface, which covers more than 70% of the Earth's surface, determine exchanges of momentum, heat and substances, influencing the global climate and the local weather state. Prediction of natural phenomena (like hurricanes) and reliable weather forecasting are fundamental for navigation, offshore structure safety and coastal protection from extreme weather conditions. Many theories have been developed to explain wave generation by wind (Miles, 1957; Phillips, 1957; Belcher and Hunt, 1993), based on different mechanisms, such as the coupling between the wind-shear and the wave critical layer, the resonance between turbulent fluctuations and wave modes, and the sheltering effect due to the wave shape. A common way to classify surface gravity waves is to distinguish between locally-generated waves (or wind waves), steeper, shorter and coupled with the local wind field, and waves that

have propagated far from their generation area (or swell waves), longer and less steep. Although simplistic, the parameter c_0/U_{ref} (or wave age), with c_0 representing the dominant wave celerity according to the linear the dispersion relation and U_{ref} representing a reference wind velocity, has been proved robust to discriminate between the two cases (Semedo et al., 2011). If the wind velocity U_{10} (measured 10-m over the water surface) is considered, a sea state characterized by the Pierson–Moskowitz spectrum is dominated by wind sea if $c_0/U_{10} < 1.2$, otherwise it is dominated by swell (Pierson, Jr. and Moskowitz, 1964; Smith et al., 1992; Alves et al., 2003).

Wind-generated waves and swell waves are generally found mixed together in the wave field. Since swell are not dependent on the local wind conditions, it is possible to find wind-generated waves and swell crossing each other with different propagation direction. A special case is represented by tropical cyclones and hurricanes, where all relative propagation directions of wind and swell can be found during a single storm (Donelan et al., 1997). There is a vast literature on wind-waves and swell interaction, but there is no consensus on the effects

E-mail address: fabio.addona@unipr.it.

of short waves on the longer carrier wave. A first theoretical treatment of secondary waves modified by primary waves was illustrated in Unna (1941, 1942, 1947), which described mechanisms of wave height increase (and possible wave breaking) of shorter waves due to the presence of longer waves. A subsequent model by Phillips (1963) emphasized the attenuation of the long wave by short waves travelling in an opposing direction. Longuet-Higgins (1969) described a maser-like mechanism responsible for long-wave growth/decay, depending on following/opposing propagation direction of the short waves, due to the action of the radiation stress on the orbital velocity of the long wave. However, Hasselmann (1971) showed that, by considering also the mass transfer (and not only the momentum balance), the global effects of short waves is to attenuate the long wave component, independently of their propagation direction. Garrett and Smith (1976) treated the same subject but, differently from (Hasselmann, 1971), they did not assume the correlation between short-wave generation and long-wave orbital velocity to be zero, with the consequence that long waves could either grow or decay depending on the wind stress and short wave amplitude distribution along the long wave phase, and on the direction of wind with respect to the long wave. Several experiments were performed to address the effects of wind on long waves (and vice versa) with contrasted results (Hatori et al., 1981; Mitsuyasu and Honda, 1982; Hsu and Hsu, 1983; Belcher et al., 1994; Thais and Magnaudet, 1996; Chen and Belcher, 2000; Grare et al., 2013; Villefer et al., 2021), again showing that mechanically-generated waves travelling through an opposing wind are attenuated (Peirson et al., 2003). Another relevant issue is the effect of mixed sea conditions on the surface drag, which is fundamental to parametrize air–sea fluxes (Donelan et al., 1997; Makin et al., 2007). Further studies have also reported that swell waves propagating against wind influence the airflow, with expected implications on air–sea fluxes (Cao et al., 2020). Theoretical and experimental works cited so far have dealt with deep-waters conditions. However, an important question that is still unsolved is how air–sea fluxes are modified when wind-generated and swell waves propagate onshore (i.e., for intermediate and shallow water conditions), that is when shoaling effects appear in the wave field (Feddersen and Veron, 2005; Shabani et al., 2014; Chen et al., 2020). It can be stated that an overall conclusion on long-wave short-waves interaction is yet to be found.

Previous studies have shown, and it is reasonable to assume, that reflection of ocean surface gravity waves becomes more relevant as they enter coastal waters. Energy from seaward (or reflected) waves has been measured up to 18% of the incident waves energy, most of which coming from low-frequency swell (Elgar et al., 1994; Baquerizo et al., 1997). Recent works investigated more in-depth into the behaviour of regular waves with a non-negligible reflected component, ruffled by wind in opposite or in following directions, through several laboratory experiments conducted in two-dimensional wave facilities. Their results have shown not only that reflection can be dominant in sustaining wave stresses, but also that the phase shift between the incident and the reflected wave must be considered to correctly interpret the wave field (Olfateh et al., 2017; Addona et al., 2018, 2020; Addona and Chiapponi, 2023). A rigorous analytical solution, supported by experimental measurements, has been found for partially-reflected regular waves, and it has been used to evaluate the wave shear stress and the radiation stress, which causes a periodic modulation of the mean water level (Addona et al., 2018). Theoretical and experimental results has indeed been shown that, when wind blows over mechanical-generated waves in both following or opposing direction, the reflected component of the long wave have a crucial effect on free surface elevation, velocity and stresses mainly close to the surface, although the effect is evident throughout the entire water column. This is particularly relevant in laboratory studies, since some usual assumptions (e.g., horizontal homogeneity and in-quadrature velocities) are no longer valid and can yield to misleading conclusions. Furthermore, conditions are not strictly uniform in x, since the total wave height varies with a double

periodicity within a wave length of the regular wave. An important element of analysis, which is missing in the previous works and is thoroughly studied in the present manuscript, is to develop the mean and phase-averaged momentum equations for partially-reflected waves, following the same procedure as (Hussain and Reynolds, 1970) and Einaudi and Finnigan (1981). In the following Section, it is shown how the new reflection-induced stress tensor emerges from the interaction between the incident and the reflected wave components, and how it is distributed along the wave phase.

A common way to tackle different effects from currents, waves and wind is to decompose the signal by applying some useful operator in the time and/or frequency domains. A very well-known technique is the triple decomposition method (see, among many others, Hussain and Reynolds, 1970; Cheung and Street, 1988; Buckley and Veron, 2016), since it splits the signal into three components (mean, periodic and fluctuating) which are then associated to the currents, the waves and the turbulence (the latter including also the wind effects, if present). The main assumption in the triple decomposition method is that the wave-induced and the fluctuating components are uncorrelated. An alternative popular method to discriminate between waves and fluctuating contribution is the linear filtering technique developed by Benilov and Filyushkin (1970), which assumes linear correlation between water surface elevation and another measured variable (e.g., velocity or pressure). A limit of the linear filtering technique is that nonlinear wave-wave interaction is seen as turbulence. Thais and Magnaudet (1996) also used a triple decomposition technique, but they further separated the contribution of wind-waves and turbulence by using the linear superposition technique developed by Donelan et al. (1992), which stems from the potential theory, overcoming the limitations from the linear filtering technique. Recently, the Proper Orthogonal Decomposition (POD), which detects the most energetic modes by choosing an optimal base, has been proposed as a technique to partition the signal into different components (Clavero et al., 2016; Addona et al., 2024).

In this paper, mechanically-generated waves which propagate in intermediate waters with an opposing wind are studied. The manuscript is developed in two directions. First, the 2D momentum equations are theoretically represented for a monochromatic wave in conditions of partial reflection, in the presence of a blowing wind. To do that, velocity and pressure variables are decomposed into a mean, a wave-incident, a wave-reflected, and a fluctuating components, the latter including both wind and turbulence (as it is also done by Cheung and Street, 1988). Then, it is shown how the 2D non-dimensional momentum equations evolve when reflection is present. Time- and phase-average operators (used for the triple decomposition) are applied to the whole momentum equations to show the mean stresses and the phase-averaged stresses, the latter intended as a distribution of the wave stresses along the wave phase. Finally, we highlight the presence of a reflection-induced stress tensor which stems from the incident-reflected wave interaction. This analysis also predicts a phase shift between the total wave height, velocity and shear stress, even when only a small fraction of reflection is present. Furthermore, the distribution of wave velocities and stresses in the phase space is represented for different reflective conditions. This scheme only takes into account reflection from the mechanically-generated waves, while it does not include possible reflection from the wind-waves field.

The second part of the paper is devoted to the experimental activity, which is used to validate the theoretical model and to analyse the fluctuating components. The experimental data presented here is the same as described in Addona and Chiapponi (2023). However, the data analysis is extended by simultaneously acquiring the free surface elevation with the velocity, so that velocity and stresses can be mapped along the mechanically-generated wave phase. The aims of the experiments are (1) to show the distribution of the periodic and fluctuating components of velocity, stresses, and kinetic energy along the phase of the mechanically-generated wave, and (2) to compare the

velocity measurements to the analytical model previously developed, which takes into account the dependence of the velocity field on the reflective conditions and on the measurements section location along x. The analysis of the water levels is not included here as it has been already reported in a previous work (see Addona et al., 2020).

The paper is divided as follows. In Section 2, a theoretical description of the momentum equations, the velocity and the stress fields is reported for progressive waves and for partially-reflected waves. Section 3 illustrates the experimental activity and the data analysis conducted, while Section 4 shows the theoretical and experimental results, with some discussions. Conclusions are depicted in Section 5, while some additional calculations are shown in the appendixes.

2. Theoretical background

2.1. Momentum equations for a progressive wave

Here, the continuity and momentum equations for an incompressible 2D flow are reported. Following a broadly used approach (see, for instance, Hussain and Reynolds, 1970; Einaudi and Finnigan, 1981), velocity and pressure are decomposed into mean, periodic, and fluctuating components:

$$
\begin{aligned}
u_i &= \bar{u}_i(x,z) + \widetilde{u}_i(x,z,\varphi) + u_i'(x,z,t), \\
p &= \bar{p}(x,z) + \widetilde{p}(x,z,\varphi) + p'(x,z,t),
\end{aligned}
\tag{1}
$$

where $i = 1,2$ stand for x and z axes, $u_1 = u$, $u_2 = w$ are the horizontal and vertical velocities, respectively, p is the pressure, and φ is the wave phase (from 0 to 2π, with 0 at the crest and π at the trough). In this case, the fluctuating component is given by the combined effects of the wind motion and of the residual turbulence, as previously done by Cheung and Street (1988). The continuity equation results:

$$
\bar{u}_{i,i} = \widetilde{u}_{i,i} = u_{i,i}' = 0,
\tag{2}
$$

where the Einstein summation convention is used and $(\dots)_{,i}$ indicates partial derivative. If the momentum equations are averaged over a time T_{ave} much larger than the wave period T, the mean momentum equations are obtained as follows:

$$
\bar{u}_{i,t} + \left(\bar{u}_j\bar{u}_i\right)_{,j} = -\frac{\bar{p}_{,i}}{\rho} - (gz)_{,i} + \left(\bar{\tau}_{ij}\right)_{,j} + \left(\bar{r}_{ij}^w + \bar{r}_{ij}^f\right)_{,j}, \qquad i = 1,2
\tag{3}
$$

where g is the gravitational acceleration, $\tau = 2\nu S$ is the kinematic viscous stress tensor, $\nu = \mu/\rho$ is the kinematic viscosity, and $S = \frac{1}{2}\left(\nabla\mathbf{u} + \nabla\mathbf{u}^T\right)$ is the strain rate tensor. The additional terms $\bar{r}_{ij}^w$ and $\bar{r}_{ij}^f$ are the kinematic mean wave-induced and fluctuating Reynolds tensors, stemming from the triple decomposition of the velocity:

$$
\begin{aligned}
\bar{r}_{ij}^w &= -\overline{\widetilde{u}_i\widetilde{u}_j} \\
\bar{r}_{ij}^f &= -\overline{u_i'u_j'}
\end{aligned}
\tag{4}
$$

The wave-induced $\widetilde{r}_{ij}^w$ and fluctuating $\widetilde{r}_{ij}^f$ tensors, which will be used in the following momentum equations, can also be defined as follows:

$$
\begin{aligned}
\widetilde{r}_{ij}^w &= -\left(\widetilde{u}_i\widetilde{u}_j + \bar{r}_{ij}^w\right) \\
\widetilde{r}_{ij}^f &= -\left(\langle u_i'u_j'\rangle + \bar{r}_{ij}^f\right),
\end{aligned}
\tag{5}
$$

where $\langle\dots\rangle$ represents a phase-average operator which acts over a wave length. The wave-induced (or periodic) momentum equations can be obtained by applying the phase-average operator at the whole momentum equations and subtracting Eq. (3):

$$
\widetilde{u}_{i,t} + \left(\bar{u}_j\widetilde{u}_i + \bar{u}_i\widetilde{u}_j\right)_{,j} = -\frac{\widetilde{p}_{,i}}{\rho} + \left(\widetilde{\tau}_{ij}\right)_{,j} + \left(\widetilde{r}_{ij}^w + \widetilde{r}_{ij}^f\right)_{,j}.
\tag{6}
$$

Finally, the fluctuating momentum equations are obtained by subtracting the mean- and periodic- to the whole momentum equations:

$$
u_{i,t}' + \left(\bar{u}_j u_i' + \bar{u}_i u_j' + \widetilde{u}_i u_j' + \widetilde{u}_j u_i'\right)_{,j} = -\frac{p'_{,i}}{\rho} + \left(\tau_{ij}'\right)_{,j} + \left(u_i'u_j' - \langle u_i'u_j'\rangle\right)_{,j}.
\tag{7}
$$

2.2. Partially-reflected waves and dimensional scaling

In the presence of partially-reflected waves, the wave-induced velocity is written as the sum of an incident and a reflected wave, i.e., $\widetilde{u}_i = \widetilde{u}_{Ii} + \widetilde{u}_{Ri}$. The time-averaged momentum equations can then be rewritten as:

$$
\bar{u}_{i,t} + \left(\bar{u}_j\bar{u}_i\right)_{,j} = -\frac{\bar{p}_{,i}}{\rho} - (gz)_{,i} + \left(\bar{\tau}_{ij}\right)_{,j} + \left(\bar{r}_{ij}^I + \bar{r}_{ij}^R + \bar{r}_{ij}^f\right)_{,j}, \qquad i = 1,2
\tag{8}
$$

where there can be defined:

$$
\begin{aligned}
\bar{r}_{ij}^I &= -\overline{\widetilde{u}_{Ii}\widetilde{u}_{Ij}}, \\
\bar{r}_{ij}^R &= -\left(\overline{\widetilde{u}_{Ii}\widetilde{u}_{Rj}} + \overline{\widetilde{u}_{Ij}\widetilde{u}_{Ri}} + \overline{\widetilde{u}_{Ri}\widetilde{u}_{Rj}}\right),
\end{aligned}
\tag{9}
$$

The term $\rho\bar{r}_{ij}^I$ is the mean wave Reynolds stress tensor induced by the incident wave, the term $\rho\bar{r}_{ij}^R$ is a new reflection-induced mean wave Reynolds tensor, and the total mean wave Reynolds tensor becomes $\rho\bar{r}_{ij}^w = \rho\left(\bar{r}_{ij}^I + \bar{r}_{ij}^R\right)$. Notice that, for $(\widetilde{u}_R, \widetilde{w}_R) = 0$, the term $\bar{r}_{ij}^R$ disappears, $\widetilde{u} = \widetilde{u}_I$ and Eq. (8) coincides with Eq. (3).

It is convenient to define a dimensional scaling for all the variables involved in the problem:

$$
\begin{aligned}
z^* &= \frac{z}{L}, \quad x^* = \frac{x}{L}, \quad t^* = \frac{t}{T}, \quad u_i^* = \frac{T}{H_T}u_i, \\
p^* &= \frac{p}{\rho g L}, \quad \tau^* = \tau\frac{LT}{H_T\nu}, \quad r_{ij}^* = \left(\frac{T}{H_T}\right)^2 r_{ij},
\end{aligned}
\tag{10}
$$

where H_T is the total wave height and k is the wave number of the mechanical wave, calculated from the linear dispersion relation. The total wave height is expressed as follows:

$$
H_T = \frac{\pi H_I}{\delta},
\tag{11}
$$

where $\delta = \pi\left(1 + K_R^2 + 2K_R\cos(\theta_I - \theta_R)\right)^{-1/2}$, see Appendix A for details. The wave phases of the incident and of the reflected components are defined as $\theta_I = kx - \omega t + \varphi_I$, $\theta_R = -kx - \omega t + \varphi_R$, where φ_I, φ_R represent their initial phases, respectively.

By substituting the dimensional scales in Eq. (8), and after some algebra, the non-dimensional mean momentum equations for partially-reflected waves read:

$$
\bar{u}_{i,t^*}^* + \epsilon\left(\bar{u}_j^*\bar{u}_i^*\right)_{,j^*} = -\frac{\alpha}{\epsilon}\left(\bar{p}^* + z^*\right)_{,i^*} + \frac{\epsilon}{Re}\left(\bar{\tau}_{ij}^*\right)_{,j^*} + \epsilon\left(\bar{r}_{ij}^{I*} + \bar{r}_{ij}^{R*} + \bar{r}_{ij}^{f*}\right)_{,j^*}
\tag{12}
$$

where $\alpha = 2\pi\coth kh > 1$, $\epsilon = H_T/L$ is a small parameter representing the wave slope, and $Re = \frac{\epsilon L^2}{T\nu}$ is the wave Reynolds number. Hereafter only non-dimensional variables are considered, so we drop the asterisk at the apex for all the terms involved.

Following the decomposition method and dimensional scaling, the non-dimensional wave-induced equations for partially-reflected waves can be written as:

$$
\widetilde{u}_{i,t} + \epsilon\left(\bar{u}_j\widetilde{u}_i + \bar{u}_i\widetilde{u}_j\right)_{,j} = -\frac{\alpha}{\epsilon}\widetilde{p}_{,i} + \frac{\epsilon}{Re}\left(\widetilde{\tau}_{ij}\right)_{,j} + \epsilon\left(\widetilde{r}_{ij}^I + \widetilde{r}_{ij}^R + \widetilde{r}_{ij}^f\right)_{,j},
\tag{13}
$$

where there can be defined:

$$
\begin{aligned}
\widetilde{r}_{ij}^I &= -\left(\widetilde{u}_{Ii}\widetilde{u}_{Ij} + \bar{r}_{ij}^I\right) \\
\widetilde{r}_{ij}^R &= -\left(\widetilde{u}_{Ii}\widetilde{u}_{Rj} + \widetilde{u}_{Ij}\widetilde{u}_{Ri} + \widetilde{u}_{Ri}\widetilde{u}_{Rj} + \bar{r}_{ij}^R\right).
\end{aligned}
\tag{14}
$$

At this stage, an analytical expression of the tensors $\bar{r}_{ij}^I$, $\bar{r}_{ij}^R$, $\widetilde{r}_{ij}^I$ and $\widetilde{r}_{ij}^R$ is needed.

2.3. The incident wave Reynolds tensor

The solution of the wave potential for a partially-reflected wave field (see Addona et al., 2018, their Eq. (9)) is used here. At the first order, the (non-dimensional) horizontal and vertical velocities of the incident wave read:

$$\widetilde{u}_I = \delta F_u \cos \theta_I,$$
$$\widetilde{w}_I = \delta F_w \sin \theta_I, \tag{15}$$

where $F_u(z) = \dfrac{\cosh k(z+h)}{\sinh kh}$ and $F_w(z) = \dfrac{\sin k(z+h)}{\sinh kh}$ represent the vertical decay, and $\theta_I(x,t) = x - 2\pi t + \varphi_I$ is the incident wave phase. The time-averaged components $\bar{r}_{ij}^I$ read:

$$\bar{r}_{11}^I = -\frac{1}{2}\delta^2 F_u^2,$$
$$\bar{r}_{12}^I = \bar{r}_{21}^I = 0, \tag{16}$$
$$\bar{r}_{22}^I = -\frac{1}{2}\delta^2 F_w^2,$$

while the wave-induced components $\widetilde{r}_{ij}^I$ read:

$$\widetilde{r}_{11}^I = -\frac{1}{2}\delta^2 F_u^2 \cos 2\theta_I,$$
$$\widetilde{r}_{12}^I = \widetilde{r}_{21}^I = \frac{1}{2}\delta^2 F_u F_w \sin 2\theta_I, \tag{17}$$
$$\widetilde{r}_{22}^I = \frac{1}{2}\delta^2 F_w^2 \cos 2\theta_I.$$

2.4. The reflection-induced wave Reynolds tensor

The solution of the reflected waves for the horizontal and vertical velocities is:

$$\widetilde{u}_R = -K_R \delta F_u \cos \theta_R,$$
$$\widetilde{w}_R = K_R \delta F_w \sin \theta_R, \tag{18}$$

where $\theta_R(x,t) = -x - 2\pi t + \varphi_R$ is the reflected wave phase. The mean reflection-induced tensor $\bar{r}_{ij}^R$ becomes:

$$\bar{r}_{11}^R = K_R \delta^2 F_u^2 \left(\cos(\theta_I - \theta_R) - \frac{1}{2}K_R \right),$$
$$\bar{r}_{12}^R = \bar{r}_{21}^R = K_R \delta^2 F_u F_w \sin(\theta_I - \theta_R), \tag{19}$$
$$\bar{r}_{22}^R = -K_R \delta^2 F_w^2 \left(\cos(\theta_I - \theta_R) + \frac{1}{2}K_R \right).$$

Notice the difference with the incident counterpart: all the terms are now dependent on the wave phase, and not strictly uniform in x anymore. Furthermore, the reflection-induced shear stress is different from zero. It is possible to find in literature other many cases where $\widetilde{u}$ and $\widetilde{w}$ are phase-shifted, resulting in a non-zero correlation $\widetilde{u}\widetilde{w}$ (Deigaard and Fredsøe, 1989; De Vriend and Kitou, 1991; Rivero and Arcilla, 1995). In the case of the present work, the out-of-quadrature velocity is induced by partial reflection conditions, i.e., K_R and $\theta_I - \theta_R$.

After some algebra, the components of the periodic $\widetilde{r}_{ij}^R$ become:

$$\widetilde{r}_{11}^R = K_R \delta^2 F_u^2 \left(\cos(\theta_I + \theta_R) - \frac{1}{2}K_R \cos 2\theta_R \right),$$
$$\widetilde{r}_{12}^R = \widetilde{r}_{21}^R = -\frac{1}{2}K_R \delta^2 F_u F_w \sin 2\theta_R, \tag{20}$$
$$\widetilde{r}_{22}^R = K_R \delta^2 F_w^2 \left(\cos(\theta_I + \theta_R) + \frac{1}{2}K_R \cos 2\theta_R \right),$$

see Appendix B for details on the calculations.

Eqs. (16)–(17)–(19)–(20) define the wave Reynolds stress tensors. In our model, p cannot be retrieved, since neither pressure nor velocity gradients were measured. Furthermore, since in the present data $\epsilon/Re \sim 10^{-6}$, viscous forces are neglected far from the interface. Thus, the following results will only focus on the velocity field and the stress tensors.

3. Experiments

The experiments were performed at the Ocean–Atmosphere Interaction Flume of the IISTA (Instituto Interuniversitario de Investigación del Sistema Tierra en Andalucia), University of Granada. The experimental apparatus consisted of a 2D wave flume coupled with a closed-loop wind tunnel, a current generator, and a wave generator, although only the wave flume and the wind tunnel were actively used during the present activity. The wind tunnel can generate airflow up to 12 m/s in only one direction. The wave flume is 16-m long and 1-m wide, equipped with two piston-type paddles for the generation and absorption of the mechanical wave located at the opposite sides of the wave flume. The control of the reflective conditions of the mechanically-generated waves was possible thanks to an active absorption/generation wave system, where the two paddles could act as wave absorbers and/or wavemakers in both directions. The active absorption method was based on digital filtering of signals acquired in the nearfield by wave gauges (Lykke-Andersen et al., 2016). The water used for the experiments was filtered freshwater with a density of $\rho = 999 \, \text{kg/m}^3$. A sketch of the experimental apparatus is shown in Fig. 1.

The laboratory tests consisted of mechanical waves ruffled by an opposing wind; the main experimental parameters are reported in Table 1. For a first set of experiments, one wind velocity and several reflective conditions of the mechanical wave (PoW1–5) were tested, meaning that the active absorption of the paddle was modified among the experiments to cover a wide range of the reflection coefficient K_R. The three-gauge method described by Mansard and Funke (1980), as modified by Baquerizo et al. (1997), was used to quantify the reflection of the monochromatic wave field near the LDV measurements section. To refer the results to the mechanically-generated wave component only, a band-pass filter was applied in the post-processing around the mechanically-generated wave frequency to the wave gauges signals (for more details on the band-pass filtering, see Addona et al., 2020). We remark that only a reflection analysis of the mechanically-generated waves, which represent the long components and are most relevant in the field, was performed. Possible reflection from wind-generated waves is not considered in the present work. A second set of experiments were then performed, for which the position of the LDV system along the flume was varied, acquiring velocities from a minimum fetch of 9.95 m (PoW2a) to a maximum fetch of 10.4 m (PoW2d). The objective of the second set of experiments was to evaluate the modulation of the wave height, velocity and stresses induced by reflection along x. The imposed wave period of the mechanically-generated wave was $T = 1.6$ s for all the experiments. The same wave period was measured by the wave gauges at the measurements section, resulting in a nominal wave length $L = 3.43$ m from the linear dispersion relation. The water depth was kept at 0.7 m for all the experiments (intermediate waters), while the remaining section available for the airflow above the water was 1.2×1 m^2. A two-component LDV system by TSI inc. was used to measure the water velocity at ten different points in the vertical between the flume bottom and the wave trough. The first point was 10 cm below the still water level, and the vertical spacing between the measurements points was 5 cm. Acquisitions of the velocity signals lasted 330 s for each point in the vertical, with an average data rate of $\approx$100 Hz for each velocity component. The free surface elevation was measured by an array of eight UltraLab ULS 80D ultrasound probes, which occupy a total fetch of $\approx$1.7 m along the flume. The wave gauges data rate was 50 Hz, with a declared spatial resolution of 0.18 mm and a reproducibility of $\pm$0.15%. One of the wave gauges was always horizontally aligned with the LDV to correlate velocity and free surface displacement. Measurements of the wind speed were performed with a Pitot tube at a fetch of 9.2 m, at six different heights from the still water level, to reconstruct the air velocity profile. Each point was acquired for $\approx$ 60 s with a data rate of 1 kHz. The air flow had a logarithmic profile (not shown here), and the Prandtl–Karman log-linear distribution was used to evaluate the air friction velocity u_{*a}. More details on the facility and the experimental activity can be found in Addona et al. (2018, 2020), Addona and Chiapponi (2023).
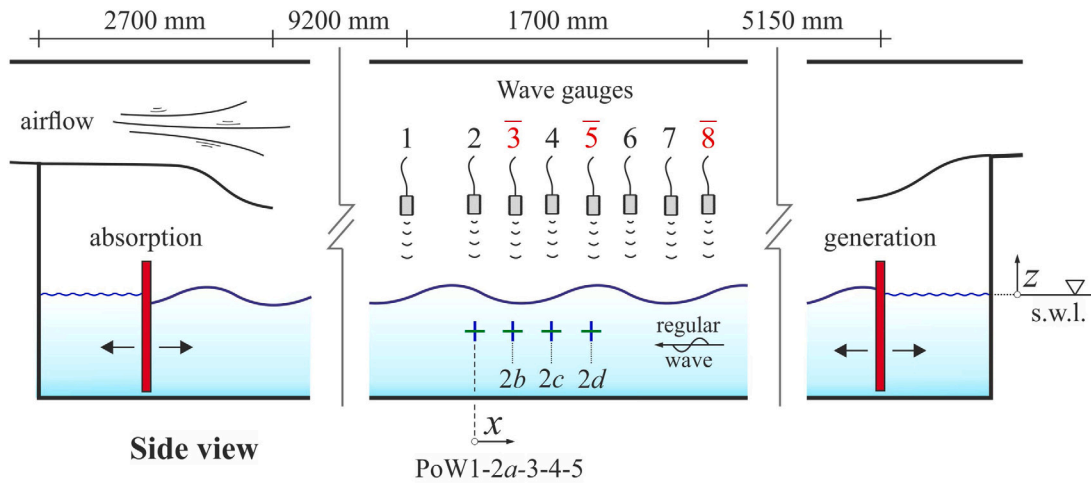
Fig. 1. A sketch of the experimental apparatus. The origin of the axes x and z is given by intersection of the first LDV measurements section (expt. PoW1-2a-3-4-5) and the still water level (s.w.l.). The dashed vertical lines starting from the "plus" signs represent the four different LDV measurements sections, as indicated by the text in the figure (PoW1-2a-3-4-5, 2b, 2c and 2d, respectively). Wave gauges 3, 5 and 8 were used for reflection analysis.

Table 1
Parameters of the experiments, consisting of mechanically-generated waves in conditions of partial reflection ruffled by an opposing wind. Notice that the possible reflection of wind-generated waves is not taken into account, and "incident" and "reflected" components only refer to the mechanically-generated waves. PoW stands for "Paddle-opposing-Wind waves"; u_{a*} is the air friction velocity obtained by fitting the log-linear profile of the airflow (measured with a Pitot tube); $u_{w*} = (\rho_a/\rho_w)^{0.5} u_{a*}$ is the water friction velocity. H_T is the total wave height, H_i is the incident wave height, T is the period of the paddle oscillation, K_r and $(\varphi_I - \varphi_R)$ are the reflection coefficient and the phase shift, respectively. The relative coordinate x/L indicates the LDV measurement section (position) with respect to US2 (see Fig. 1).

Expt.	u_{a*} (cm s^{-1})	u_{w*} (cm s^{-1})	x/L	H_T (cm)	H_i (cm)	T (s)	$K_{r,w}$	$\varphi_I - \varphi_R$ (rad)
PoW 1	75	2.6	0	5.5 ± 0.1	3.8 ± 0.1	1.6	0.74 ± 0.01	1.10 ± 0.10
2a	75	2.6	0	5.7 ± 0.1	4.3 ± 0.1	1.6	0.60 ± 0.01	1.15 ± 0.03
2b	75	2.6	0.04	6.6	4.3	1.6	0.61	1.15
2c	75	2.6	0.09	6.9	4.3	1.6	0.61	1.12
2d	75	2.6	0.13	6.7	4.3	1.6	0.61	1.11
3	75	2.6	0	5.6	5.3	1.6	0.30	1.36
4	75	2.6	0	5.1	5.4	1.6	0.12	1.78
5	75	2.6	0	4.8	5.3	1.6	0.07	1.89

3.1. Data analysis

The main novelty of the experimental data analysis, if compared to Addona and Chiapponi (2023), is that velocity and free surface measurements were retrieved simultaneously. Having both measurements at the same time, a band-pass filter was used during the post-processing in the frequency domain of the surface elevation variations signals to obtain the periodic component $\tilde{\eta}$. Then, the velocity measurements were associated to the phase of the mechanical wave by applying a Hilbert transform to $\tilde{\eta}$, where the "zero" phase corresponds to the wave crest. The procedure is similar to the one by Buckley and Veron (2016), although they worked in the space domain.

A triple decomposition was applied to the velocity measurements to obtain mean, periodic and fluctuating components (same as Eq. (1)). The procedure is fully described in Addona and Chiapponi (2023) and it is here briefly reported. First, the temporal average of the signal gives the mean (current) component:

$$\bar{u}_i(x,z) = \frac{1}{T_{acq}} \int_0^{T_{acq}} u_i(x,z,t)\mathrm{d}t, \tag{21}$$

where T_{acq} is the acquisition duration. As a second step, the periodic component is obtained by phase-averaging the whole signal and subtracting the mean value:

$$\tilde{u}_i(x,z,\tau) = \langle u_i - \bar{u}_i \rangle = \frac{1}{N}\sum_{j=1}^{N}\left(u_i(x,z,\tau+jT)\right) - \bar{u}_i(x,z), \tag{22}$$

where T is the mechanical wave period, τ is the mechanical wave phase and N is the total number of waves observed in one test. It

has been verified that the mechanical wave period is exactly 1.6 s for each incoming wave, both near the wave generation area and near the measurements section. Notice that experimentally, with this procedure, only the sum of the incident and the reflected wave velocities, i.e., the total periodic component, can be determined, but it is not possible to evaluate each term separately. Finally, subtracting the mean and the periodic velocities from the whole signal yields the fluctuating component:

$$u_i'(x,z,t) = u_i(x,z,t) - \bar{u}_i(x,z) - \tilde{u}_i(x,z,\tau). \tag{23}$$

This technique has been proven effective in separating the periodic component, as shown in previous works (Cheung and Street, 1988; Olfateh et al., 2017; Addona et al., 2018, 2020; Addona and Chiapponi, 2023, to cite only a few). The mean and phase-average operators are also applied to the wave stresses $\rho u_i u_j$ to obtain the Reynolds stress tensors, both for the wave-induced ($\bar{r}_{ij}^w$ and $\tilde{r}_{ij}^w$) and for the fluctuating ($\bar{r}_{ij}^f$ and $\tilde{r}_{ij}^f$) components.

4. Results and discussion

4.1. Considerations about the dimensional scaling and the total wave components

From our dimensional scaling, it is found that $u_i \sim \delta$ and $r_{ij} \sim \delta^2$. Fig. 2 reports δ as a function of x, K_R and $\varphi_I - \varphi_R$ separately. It is possible to observe in panels (a) and (c) that the functions abruptly increase for some values of x/L and $\varphi_I - \varphi_R$; as it was easily predictable,
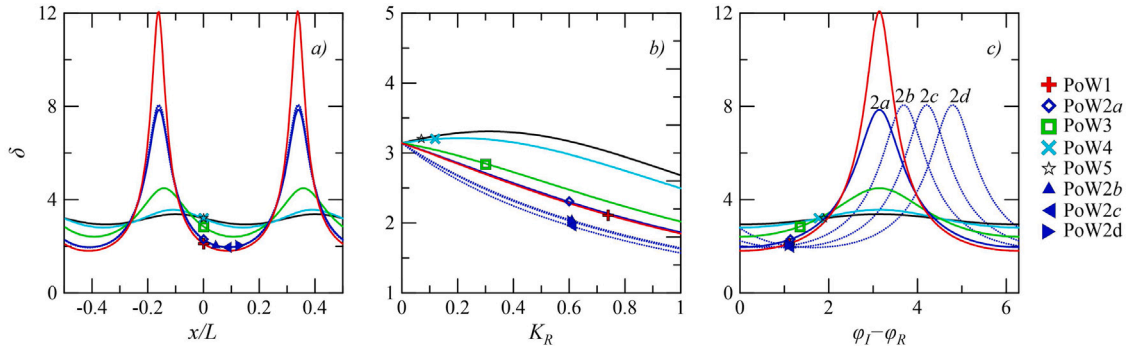
Fig. 2. Variation of δ as a function of the measurements section x (panel a), of the reflection coefficient K_R (panel b), and of the phase shift $\varphi_I - \varphi_R$ (panel c). Curves represents theoretical values, while symbols stems from experimental conditions. Red, blue, green, cyan and black refer to PoW1, PoW2a–d (b–d are dashed curves), PoW3, PoW4, and PoW5, respectively.

it happens near the nodes, where the total wave height goes to zero and the scaling cannot be used anymore. It is also possible to observe that for $K_R \rightarrow 0$, δ tends to a constant value. Laboratory studies usually assume that reflection below a certain threshold (e.g., 5 or 10% of the incident wave height) is negligible, although in our data the modulation of δ is still present for PoW5 ($K_R = 0.07$). This scaling shows that, even for K_R relatively small, it is not enough to take into consideration only the reflection coefficient K_R (i.e., the ratio of the reflected to the incident wave height) to infer the effects of reflection on the flow. In fact, the resulting wave field is conditioned by the other two factors: the phase shift between the incident and the reflected waves ($\varphi_I - \varphi_R$) and the position of the measurements section along the wave flume (x/L), which are linked to the long-wave phase and cannot be determined without a thorough reflection analysis. Although this study only focuses on a monochromatic mechanically-generated wave, it may be inferred that every wave field should be treated with care when dealing with reflective conditions.

The total wave velocity and shear stress are given as the sum of the incident and reflected components, i.e., $\tilde{u} = \tilde{u}_I + \tilde{u}_R$ and $\tilde{r}_{12}^w = \tilde{r}_{12}^I + \tilde{r}_{12}^R$. However, it is possible to apply the same method used in Appendix A to express both quantities as a single sinusoidal function as follows

$$\tilde{u} = U \cos\left(x - 2\pi t + \gamma_t\right), \tag{24}$$

$$\tilde{r}_{12}^w = R \sin\left(2x - 4\pi t + \Omega_t\right), \tag{25}$$

where U, γ_t and R, Ω_t are the amplitudes and the initial phases of the total wave velocity and of the total shear stress, respectively. After some algebra and trigonometry, it is found that

$$U = \delta F_u \left(1 + K_R^2 - 2K_R \cos\left(2x + \theta_I - \theta_R\right)\right)^{1/2},$$
$$\gamma_t = \arctan \frac{\sin\varphi_I' - K_R \sin\varphi_R'}{\cos\varphi_I' - K_R \cos\varphi_R'}, \tag{26}$$

for the total velocity, and

$$R = \frac{1}{2}\delta^2 F_u F_w \left(1 + K_R^2 - 2K_R \cos\left(4x + 2\theta_I - 2\theta_R\right)\right)^{1/2},$$
$$\Omega_t = \arctan \frac{\sin 2\varphi_I' - K_R \sin 2\varphi_R'}{\cos 2\varphi_I' - K_R \cos 2\varphi_R'}, \tag{27}$$

for the total wave shear stress, valid when the denominators of Eqs. (26)–(27) are different from 0. We see that, generally speaking, $\varphi_t \neq \gamma_t \neq \Omega_t$. For the velocity, this is due to the fact that the horizontal velocity u changes sign depending on the wave propagation direction, i.e., incident or reflected.

The phase-averaged shear stress is given as the sum of the mean and the wave-induced shear stresses $\langle r_{12}^w \rangle = \bar{r}_{12}^w + \tilde{r}_{12}^w$, i.e., it can be easily obtained if it is added to Eq. (25) a constant exactly equal to $\bar{r}_{12}$. The phase-averaged term is introduced here because it is used when comparing the wave shear stress with the experimental results.

Fig. 3 shows how the initial phases of the total wave height, of the total wave velocity and of the total wave shear stress vary (i) for expts. 2a–d, as a function of x/L (panel a), and (ii) for expts. PoW1–5, as a function of K_R (panel b). In particular, it is possible to notice that the values of φ_t, γ_t and Ω_t tends to converge to zero for $K_R = 0$, i.e., for no reflection. The "zero" reference for the initial phases are the initial phase φ_I of the incident wave, so that everything collapses to a single progressive wave in the absence of reflection, as expected.

In summary, it has been observed that, for partially-reflected waves, $\varphi_t \neq \gamma_t \neq \Omega_t$ (i.e., different initial phases). The physical meaning is that there is a phase shift between the wave height, the wave velocity and the wave shear stress. This is relevant when modelling the interaction between short gravity waves and long waves, since in some analytical models (see, for instance, Longuet-Higgins and Stewart, 1960) it has been assumed that the wave velocity is in phase with the free surface elevation. From that assumption, several results were derived about the interaction between short wind-waves and long mechanically-generated wave, in terms of wave length, celerity and amplitude of the short wind-waves. By introducing a phase shift, one should expect that the interaction of wind-waves and partially-reflected long waves would be affected. Furthermore, the values of velocity and shear stress at the surface influence the kinematic and dynamic boundary conditions, thus it is fundamental to correctly predict both quantities (i.e, the modulus and the phase shift of wave height, velocities and stresses).

4.2. The distribution of the incident and reflected wave velocity and stresses

Fig. 4 reports the distribution of the incident, the reflected and the total wave horizontal velocity for PoW1 and PoW5, i.e., the maximum and the minimum reflection, respectively. The reflected component has higher (absolute) values for higher reflection, as expected. Notice that the incident and the reflected components are in phase with the incident and the reflected waves, respectively, but the reflected wave has an opposite sign (since it is propagating in the negative x direction). The total wave, given by the sum of the incident and the reflected components, has a modulus which is comparable with the incident wave. However, a phase shift between the total wave elevation and the total wave velocity can be observed, which is more relevant for higher reflection, as reported in Section 4.1 and illustrated in Fig. 3.

The partitioning of the incident and reflected phase-averaged shear stress is reported in Fig. 5 for the maximum and minimum reflective conditions (PoW1 and PoW5, respectively). As expected, it is observed a double periodicity of the shear stresses along the regular wave phase. The incident component $\langle r_{12}^I \rangle$ is symmetric, thus it does not contribute to the total mean shear stress. On the contrary, $\langle r_{12}^R \rangle$ stems from the correlation $-\tilde{u}_R \tilde{w}_R$, which is symmetric, and a constant contribution, given by interaction between the incident and the reflected velocities, i.e., $-(\tilde{u}_I \tilde{w}_R + \tilde{w}_I \tilde{u}_R)$. The last term determines the mean wave shear
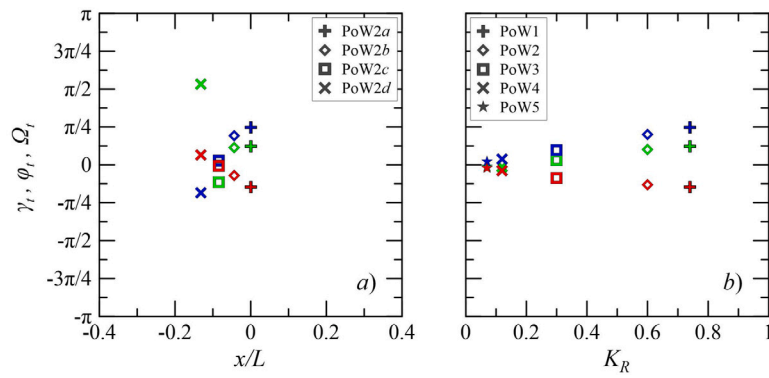
Fig. 3. Variation of the initial phases of the total wave height φ_t (red symbols), of the total wave velocity γ_t (blue symbols) and of the total wave shear stress Ω_t (green symbols), as a function of the measurements section x/L (panel a) and of the reflection coefficient K_R (panel b).
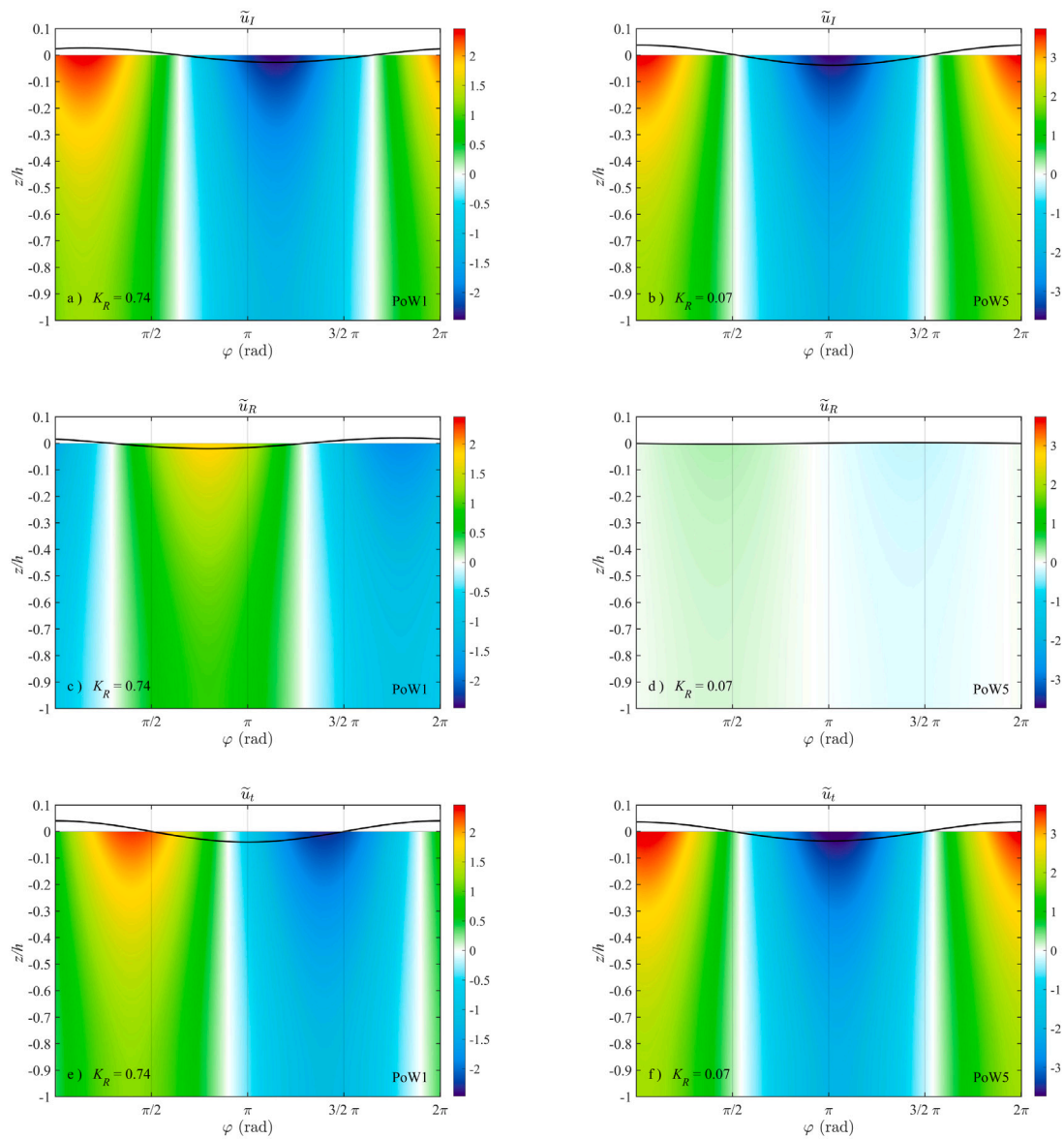

Fig. 4. Horizontal velocity components: incident $\tilde{u}_I$ (panels a–b), reflected $\tilde{u}_R$ (panels c–d) and total $\tilde{u}_t$ (panels e–f) for maximum reflection (PoW1, panels a–c–e), and minimum reflection (PoW5, right panels b–d–f), as a function of the phase φ of the total wave. Black curves represent the incident (panels a–b), reflected (panels c–d) and total wave shape.
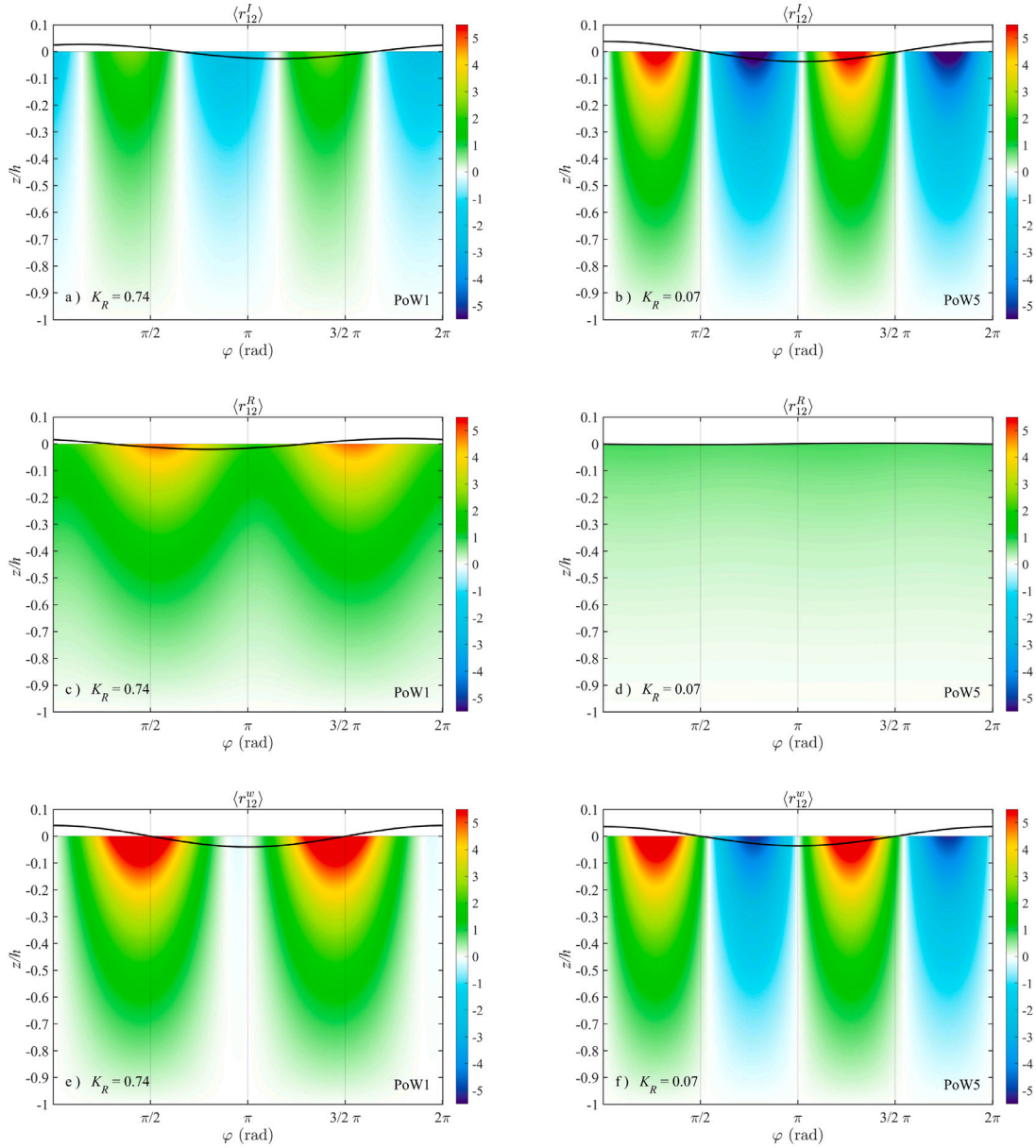
Fig. 5. Phase-averaged wave shear stress: incident $\langle r_{12}^I \rangle$ (panels a–b), reflected $\langle r_{12}^R \rangle$ (panels c–d) and total $\langle r_{12}^w \rangle = \langle r_{12}^I \rangle + \langle r_{12}^R \rangle$ (panels e–f) for maximum reflection (PoW1, left panels a–c–e), and minimum reflection (PoW5, right panels b–d–f), as a function of the phase φ of the total wave. The phase-averaged shear stresses are calculated as $\langle r_{12} \rangle = -\widetilde{u}\widetilde{w} = \overline{r}_{12} + \widetilde{r}_{12}$ (see Eq. (5)). Black curves represent the incident (panels a–b), reflected (panels c–d) and total wave shape.

stress, and it is different from zero only in the total absence of reflection, which rarely happens in real conditions, both in the field and in laboratory.

It is useful to compare the experimental and theoretical results as a check of our theoretical model and of our experimental method. We highlight that an LDV technique has been used at several vertical positions to reconstruct the experimental velocity and shear stress along the regular wave phase. Furthermore, a linear technique (phase average, Eq. (22)) has been applied to separate the contribution of the periodic component, which is not able to account for the non-linear terms emerging from the interaction between the wind and the mechanically-generated wave. Figs. 6 and 7 show the comparison of the horizontal total wave velocity and phase-averaged total shear stresses, respectively, for different reflective conditions (expts PoW1–3–4–5, notice the different velocity scales for different experiments). Even considering all the limitations and assumptions listed before, the overlap is remarkably good for all the conditions, with some discrepancy in phase and intensity for only a few points in the observed

domain. It can be seen that, for reflective conditions going to zero, the total horizontal velocity $\widetilde{u}$ tends to the values of a progressive wave. The interaction between incident and reflected waves results in highly asymmetrical total shear stress $\widetilde{r}_{12}$ for strong reflective conditions. Then, for decreasing reflection the total shear stress progressively tends to a symmetric distribution, resulting in zero values below the nodes, the crest and the trough.

4.3. The distribution of the fluctuating stresses and TKE

We do not present here a model to obtain the fluctuating components of the velocity and stresses, where the term "fluctuating" includes both the wind and the turbulence contribution. However, the fluctuating components are experimentally evaluated from the LDV measurements by means of the triple decomposition technique, see Eq. (23). In this sub-section, the attention is focused on the distribution of the fluctuating stresses and energy.
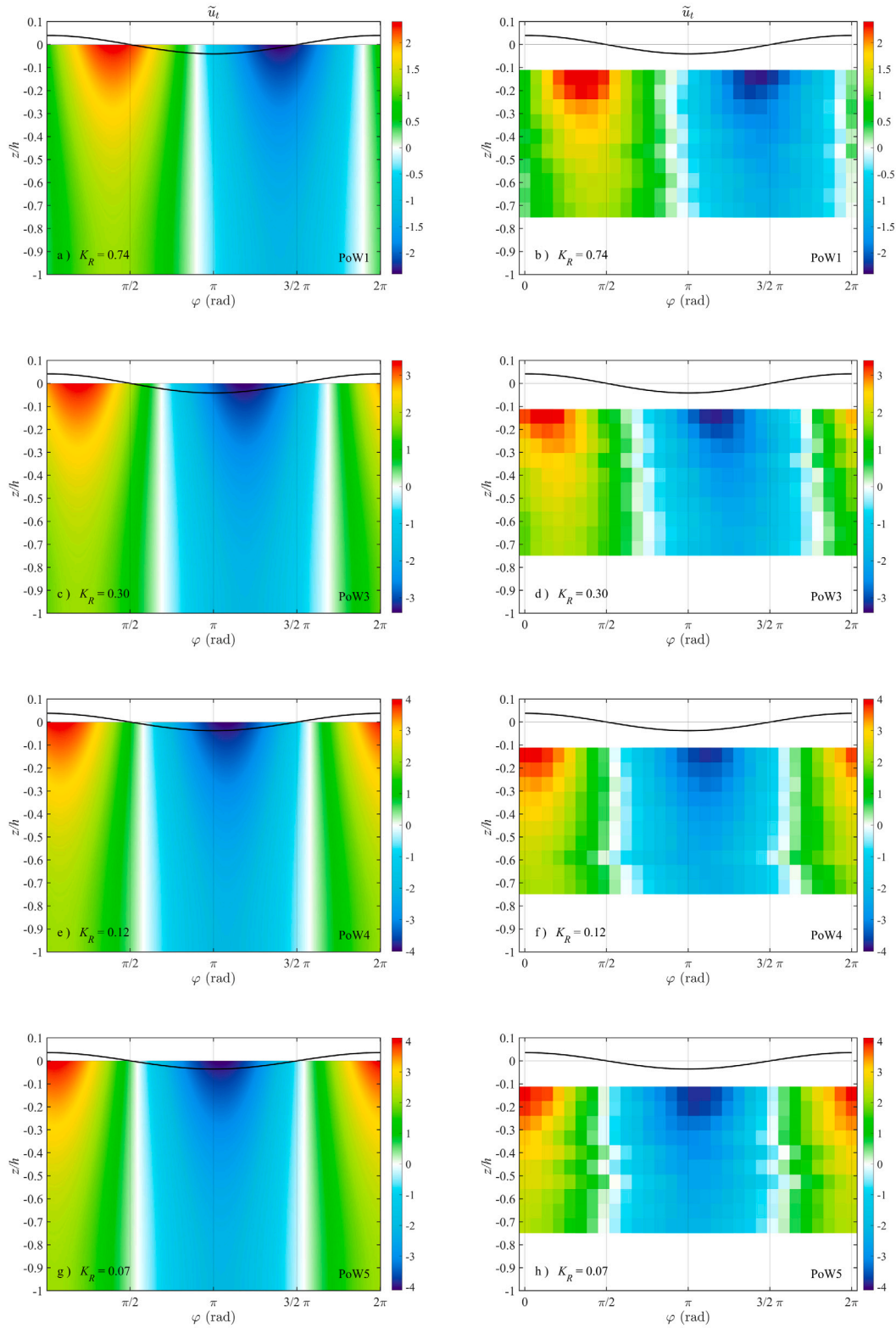
Fig. 6. Horizontal velocity $\tilde{u}_t$ for decreasing reflective conditions (from PoW1, upper panels to PoW5, lower panels). The LDV measurements section is at $x = 0$ for all the tests reported here. Left panels represent theoretical values, right panels represent experimental values. Black curves represent the total wave shape.

Here a different normalization is chosen for the vertical coordinate. Instead of a fixed z/h, the local depth $z' = z - \eta_t$ is used for the measured point, and $h' = h + \eta_t$ is used for the total water depth, resulting in a new non-dimensional vertical coordinate z'/h'. As a consequence, points

below the crest will be mapped at greater depths, while points below the trough will be mapped closer to the surface, which is represented by $z'/h' = 0$. The new mapping is similar to curvilinear coordinate systems with a vertical decay, which are frequently used to better represent
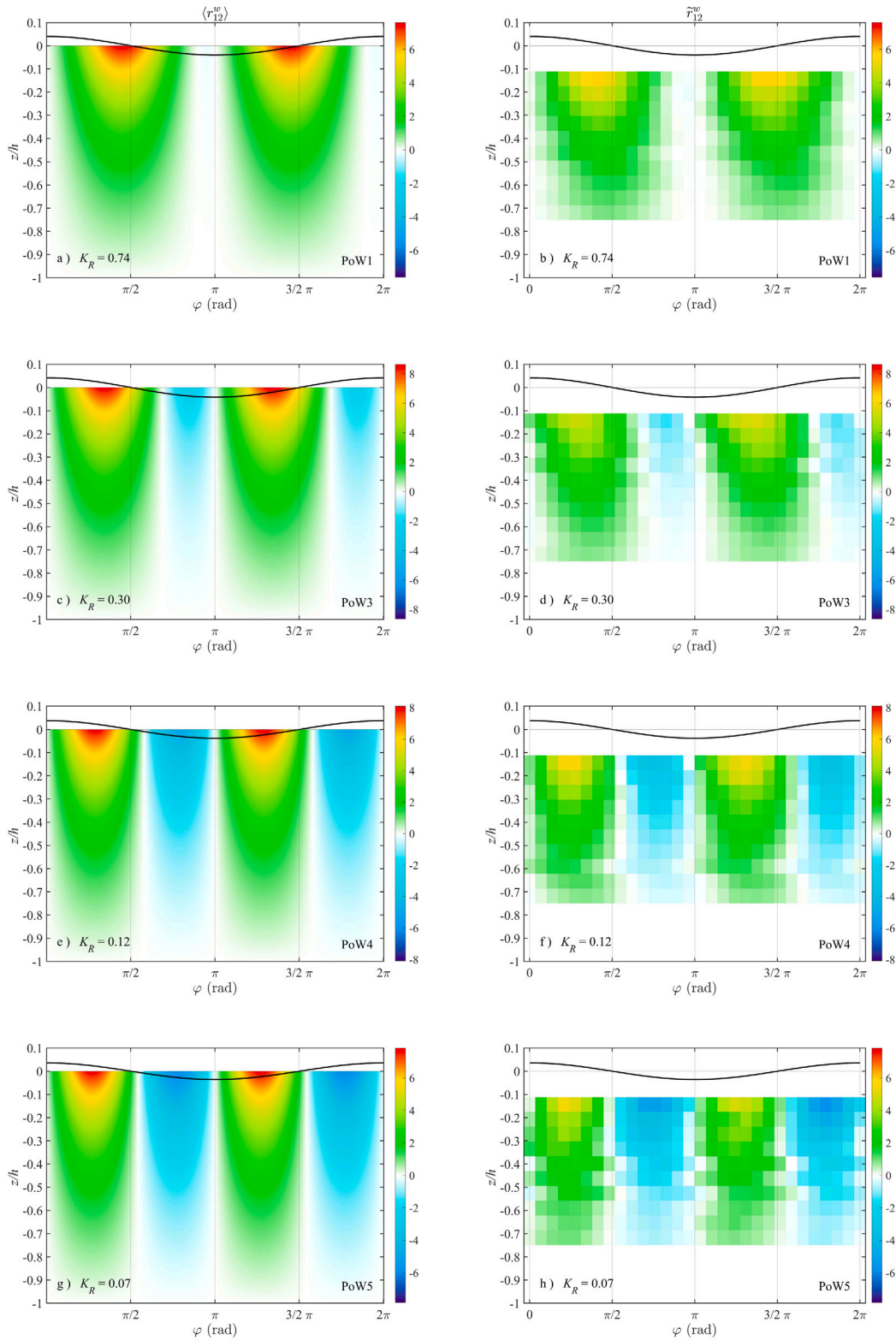
Fig. 7. Phase-averaged total wave shear stress $\langle r_{12}^w \rangle = \langle r_{12}^I \rangle + \langle r_{12}^R \rangle$ for decreasing reflective condition (from PoW1, upper panels to PoW5, lower panels). Left panels represent theoretical values, right panels represent experimental values. Black curves represent the total wave shape.

data in the region between the crest and the trough (see, for instance, Buckley and Veron, 2016). As it is shown in the following results, it allows to emphasize the depth of the measured points with respect to the local free surface elevation, which varies as a function of the wave phase.

Fig. 8 reports how the experimental phase-averaged Reynolds shear stress $\langle r_{12}^f \rangle$ varies for different reflective conditions (PoW1 and PoW5)

and for varying LDV measurements sections (PoW2a and PoW2d). The discontinuities in the images derive from the discretization of the wave domain and the low vertical resolution, making the fluctuating components appear more chaotic. In any case, the distribution of $\langle r_{12}^f \rangle$ along the mechanically-generated wave phase shows an overall momentum transfer from air to water, i.e., a positive $\langle r_{12}^f \rangle$, and higher values in the proximity of the interface. For higher reflective conditions ($K_R = $
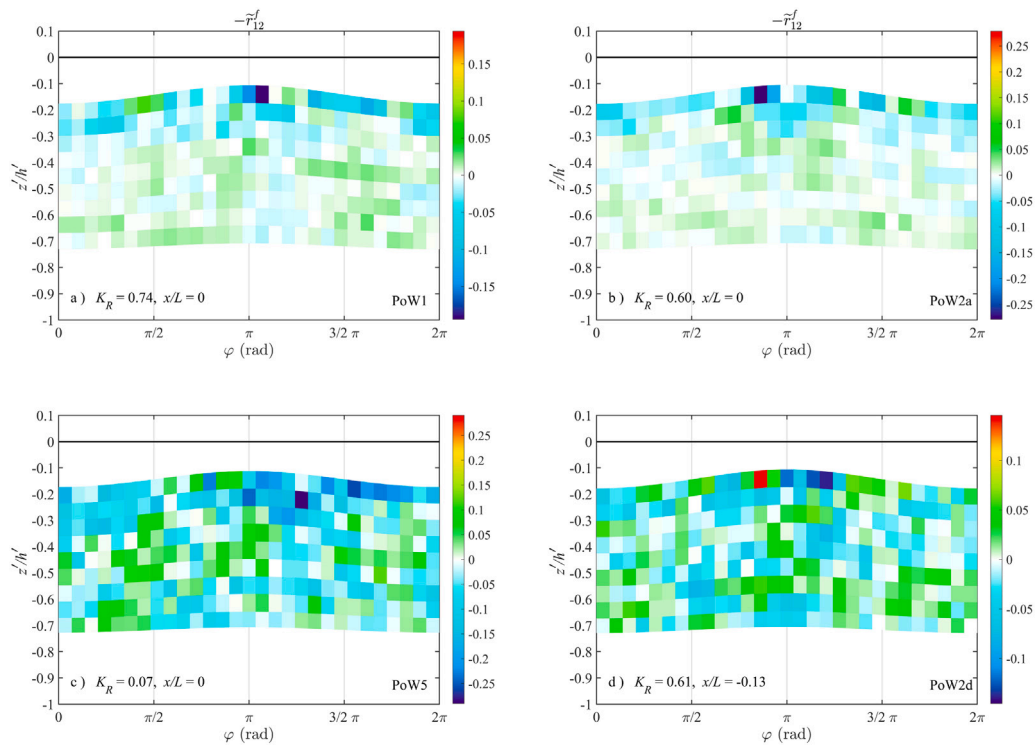
Fig. 8. Experimental phase-averaged fluctuating shear stress $-\langle r_{12}^f \rangle = -\left(\bar{r}_{12}^f + \tilde{r}_{12}^f \right)$, with the new vertical normalization z'/h'. Panels a–c show the maximum and the minimum reflection coefficient K_R (PoW1 and PoW5, respectively), while panels b–d show the farthest LDV measurements along x section (PoW2a and 2d, respectively, with K_R constant), as a function of the phase φ of the total wave. Black curves represent the total wave shape.

$0.6 - 0.74$), the maximum shear stress is located near the trough, while for $K_R = 0.07$ there is a higher contribution on the upwind side of the wave, close to the wave crest. On the other hand, there is not a clear dependence of $\langle r_{12}^f \rangle$ on x/L (panels b and d).

Fig. 9 shows the experimental fluctuating kinetic energy TKE along the mechanical wave phase, again for different reflective conditions (PoW1 and PoW5) and for different LDV measurements sections (PoW2a and PoW2d). Highest values of TKE can be observed closer to the free surface, with maximum values around the wave trough and a rapid decay far from the interface. The distribution of TKE along the regular wave phase does not look strongly affected by varying $K_R, \theta_I - \theta_R$ and x/L. However, it can be noticed that the condition of minimum reflection (PoW5) has higher non-dimensional values of TKE, with a slight phase shift upwind.

Physically, in condition of minimum reflection, the highest intensity of the fluctuating stresses and energy upwind could be explained by the mechanism depicted by previous works (Longuet-Higgins and Stewart, 1960; Phillips, 1963; Hasselmann, 1971), which predicted a steepening of the wind-waves in proximity of the wave crest. Higher reflection seems to damp the steepening effect, with a symmetric distribution of both $\langle r_{12}^f \rangle$ and TKE with respect to the wave trough (PoW1). Furthermore, the new normalization of the vertical coordinate (z'/h') highlights that the measured $\langle r_{12}^f \rangle$ and TKE are closer to the free surface below the trough, while they are farther below the crest. Since the wind forcing acts at the surface, the phase-dependent depths of the measurements could partly explain why we observe highest intensities of the fluctuating stresses and energy near the wave trough. In any case, it is still possible to observe a modulation of the fluctuating stresses and energy as a function of the reflective conditions.

5. Conclusions

We report on a theoretical and experimental study of a partially-reflected regular wave field in the presence of an opposing wind. As

in lab setup is very hard but possible to avoid reflection, while in any coastal zone reflections will always be present, it is important to know how partially-reflected waves differ from a single progressive wave to correct possible contamination and wrong interpretations of the results.

A theoretical analysis is started by splitting the variables into mean, incident wave, reflected wave and fluctuating components. After substituting the decomposed quantities directly in the momentum equations, time- and phase-average operators are applied to define the mean and the wave-induced momentum equations. A new reflection-induced stress tensor is defined, given by the interaction between the incident and the reflected wave field. It is also introduced a dimensional scaling which is a function of the total wave height and the wave period, where the non-dimensional variable δ faithfully represents velocity and stresses. One of the effects of partial reflection is to modulate the total wave height along x, so the scaling is valid far from the nodes (since the total wave height tends to zero at the nodes). From the solution for partially-reflected waves reported in Addona et al. (2018), it is possible to quantify the correlation of the incident and the reflected waves along the phase of the total wave as a function of the reflective conditions (i.e., the reflection coefficient K_R, and the phase shift $\theta_I - \theta_R$ between the incident and the reflected wave). The total wave elevation, the total wave velocity and the total wave shear stress (given as the sum of the incident and the reflected components), are strongly dependent on the incident-reflected waves interaction. The total quantities are expressed as a single sinusoidal function, with an amplitude and a phase. In that way, it is shown that, for general values of K_R and $\theta_I - \theta_R$, the free surface, the velocity and the stresses are not in phase anymore, thus determining different kinematic and dynamic boundary conditions at the interface if compared to a single progressive wave. Furthermore, the solution shows that the analysed wave field is also dependent on x; from an operational point of view, it means that much attention must be paid for the location of the measurements section along the wave flume.

Experimentally, the free surface elevation was measured with ultrasound wave gauges, while velocity was measured with the Laser
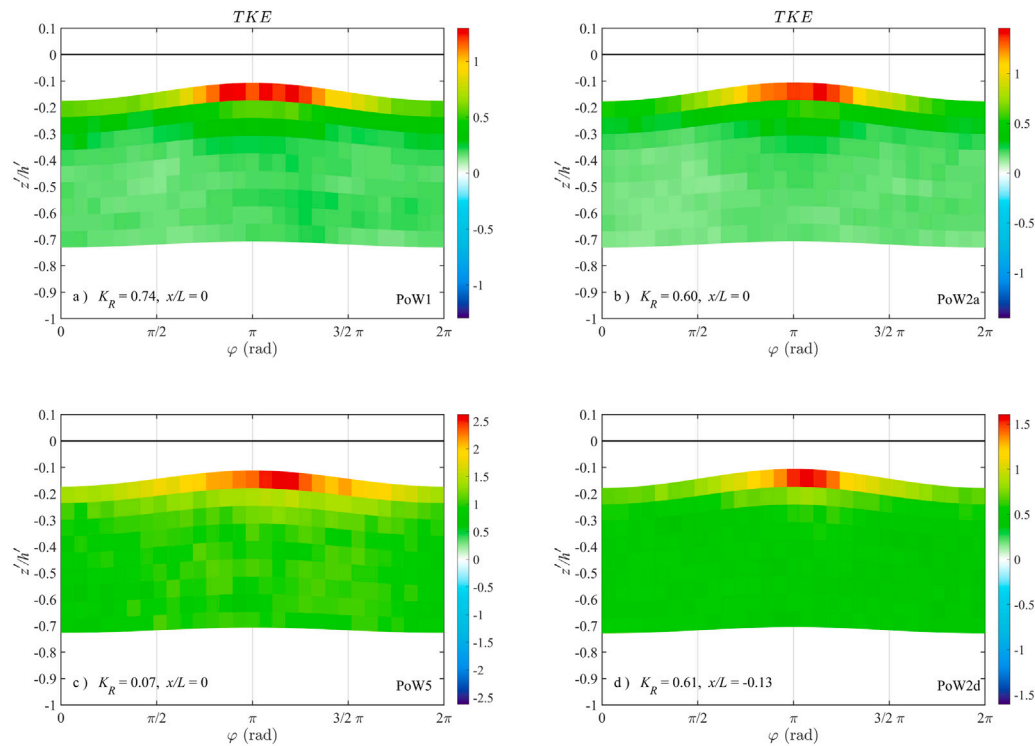
Fig. 9. Phase-averaged experimental fluctuating kinetic energy $TKE = \langle u'^2 + w'^2 \rangle / 2$, with the new vertical normalization z'/h'. Panels a–c show the maximum and the minimum reflection coefficient K_R (PoW1 and PoW5, respectively), while panels b–d show the farthest LDV measurements along x section (PoW2a and 2d, respectively, with K_R constant), as a function of the phase φ of the total wave. Black curves represent the total wave shape.

Doppler Velocimetry technique at ten different depths. Time- and phase-average operators are applied as for the theoretical analysis to split the signal through a triple decomposition. In the experimental case, the periodic term includes both the incident and the reflected waves, while the fluctuating term indicates the overall effect of wind and turbulence. The reflection analysis is performed only for the monochromatic wave, while possible reflection from wind-generated waves is not considered. By synchronizing velocity and free surface measurements, it is possible to reconstruct the phase-averaged experimental velocity and stresses, i.e., the distribution of the periodic and fluctuating components along the regular wave phase, which is the main novelty of the experimental work. The agreement between the experimental results and the theoretical model is remarkably good, thus suggesting a satisfactory accuracy of the analytical solutions and of the experimental procedure. The variation of the fluctuating shear stress and kinematic energy (TKE) is also observed as a function of the reflective conditions. The negative values of the Reynolds shear stress indicate a momentum transfer from the air to the water, with higher values in proximity of the interface (which is expected, since the forcing acts at the surface). The TKE is also higher close to the free surface, with a rapid vertical decay for increasing water levels. For higher reflective conditions ($K_R = 0.6 - 0.74$), the Reynolds shear stress and TKE show maximum values near the wave trough, which is also where the measurements point is closer to the free surface. For the minimum reflective condition ($K_R = 0.07$), the Reynolds shear stress is more intense and the maximum values are phase-shifted upwind, close to the crest, which is consistent with a wind-wave steepening due to short-wave long-wave interaction effect (see Longuet-Higgins and Stewart, 1960; Phillips, 1963; Hasselmann, 1971). For the same low reflection, the TKE also presents higher intensity, but the phase shift of the maximum is less evident. Differently from the phase-averaged quantities, the fluctuating shear stress and the TKE do not show a clear dependence on x.

A further step of the data analysis, which is left for a future work, could be to use the results mapped in the wave phase space to evaluate the gradients of the velocity and the divergence of the stresses, with the final aim to close the balance for the 2D momentum equations.

CRediT authorship contribution statement

Fabio Addona: Writing – review & editing, Writing – original draft, Visualization, Validation, Software, Methodology, Investigation, Formal analysis, Data curation, Conceptualization.

Declaration of competing interest

The authors declare that they have no known competing financial interests or personal relationships that could have appeared to influence the work reported in this paper.

Data availability

Data will be made available on request.

Acknowledgements

Appendix A. The total wave elevation

At the first order, the total wave elevation in the presence of an incident and a reflected wave reads:

$$\eta_t = a_I \big(\cos(kx - \omega t + \varphi_I) + K_R \cos(-kx - \omega t + \varphi_R) \big). \tag{28}$$

with φ_I, φ_R the initial phase of the incident and of the reflected waves, respectively. We want to write η_t as a sinusoidal wave in the form:

$$\eta_t = a_t \cos \theta_t, \tag{29}$$

where $\theta_t = kx - \omega t + \varphi_t$. Using trigonometric formulas we obtain:

$$\begin{aligned} a_t \cos \varphi'_t &= a_I \left(\cos \varphi'_I + K_R \cos \varphi'_R \right) \\ a_t \sin \varphi'_t &= a_I \left(\sin \varphi'_I + K_R \sin \varphi'_R \right), \end{aligned} \tag{30}$$

where $\varphi'_t = kx + \varphi_t$, $\varphi'_I = kx + \varphi_I$ and $\varphi'_R = -kx + \varphi_R$. Then, we obtain:

$$\begin{aligned} a_t &= a_I \sqrt{1 + K_R^2 + 2 K_R \cos(2kx + \varphi_I - \varphi_R)} \\ \varphi_t &= \arctan \left(\frac{\sin \varphi'_I + K_R \sin \varphi'_R}{\cos \varphi'_I + K_R \cos \varphi'_R} \right) - kx, \end{aligned} \tag{31}$$

valid when $\cos \varphi'_I + K_R \cos \varphi'_R \neq 0$. Thus, given the wave number k, the total wave elevation phase depends on two factors: i) the reflection conditions, i.e., K_R, φ_I and φ_R, and (ii) the location x. Generally speaking, it differs from the incident and reflected wave phases. The total wave height, used for dimensional scaling, reads:

$$H_t = H_I \sqrt{1 + K_R^2 + 2 K_R \cos(\theta_I - \theta_R)}, \tag{32}$$

where we have defined $\theta_I = kx - \omega t + \varphi_I$ and $\theta_R = -kx - \omega t + \varphi_R$ as the incident and reflected wave phases, respectively.

Appendix B. The wave Reynolds stress components

We report here the extended calculations for the incident and reflection-induced Reynolds stress tensors. First, we write down all the terms involved in the calculations, represented by the velocity covariances that are averaged in time $(\overline{\widetilde{u}_i \widetilde{u}_j})$ and over a wave length $(\widetilde{u_i u_j})$. The mean components read:

$$\begin{aligned} \overline{\widetilde{u}_I^2} &= \delta^2 F_u^2 \overline{\cos^2 \theta_I} = \frac{1}{2} \delta^2 F_u^2, \\ \overline{\widetilde{u}_I \widetilde{w}_I} &= \delta^2 F_u F_w \overline{\sin \theta_I \cos \theta_I} = 0, \\ \overline{\widetilde{w}_I^2} &= \delta^2 F_w^2 \overline{\sin^2 \theta_I} = \frac{1}{2} \delta^2 F_w^2, \\ \overline{\widetilde{u}_I \widetilde{u}_R} &= K_R \delta^2 F_u^2 \overline{\cos \theta_I \cos \theta_R} = -\frac{1}{2} K_R \delta^2 F_u F_w \cos(\theta_I - \theta_R), \\ \overline{\widetilde{u}_R^2} &= K_R^2 \delta^2 F_u^2 \overline{\cos^2 \theta_R} = \frac{1}{2} K_R^2 \delta^2 F_u^2, \\ \overline{\widetilde{u}_I \widetilde{w}_R} &= K_R \delta^2 F_u F_w \overline{\sin \theta_R \cos \theta_I} = -\frac{1}{2} K_R \delta^2 F_u F_w \sin(\theta_I - \theta_R) \\ \overline{\widetilde{w}_I \widetilde{u}_R} &= -K_R \delta^2 F_u F_w \overline{\sin \theta_I \cos \theta_R} = -\frac{1}{2} K_R \delta^2 F_u F_w \sin(\theta_I - \theta_R), \\ \overline{\widetilde{u}_R \widetilde{w}_R} &= K_R^2 \delta^2 F_u F_w \overline{\sin \theta_R \cos \theta_R} = 0, \\ \overline{\widetilde{w}_I \widetilde{w}_R} &= K_R \delta^2 F_w^2 \overline{\sin \theta_I \sin \theta_R} = \frac{1}{2} K_R \delta^2 F_w^2 \cos(\theta_I - \theta_R), \\ \overline{\widetilde{w}_R^2} &= K_R^2 \delta^2 F_w^2 \overline{\sin^2 \theta_R} = \frac{1}{2} K_R^2 \delta^2 F_w^2. \end{aligned} \tag{33}$$

Notice that the term $(\theta_I - \theta_R)$ implies periodicity in space, but it is constant when averaged in time. The phase-averaged components of

the velocity covariances become:

$$\begin{aligned} \widetilde{u}_I^2 &= \delta^2 F_u^2 \cos^2 \theta_I = \frac{1}{2} \delta^2 F_u^2 (1 + \cos 2\theta_I), \\ \widetilde{u}_I \widetilde{w}_I &= \delta^2 F_u F_w \sin \theta_I \cos \theta_I = \frac{1}{2} \delta^2 F_u F_w \sin 2\theta_I, \\ \widetilde{w}_I^2 &= \delta^2 F_w^2 \sin^2 \theta_I = \frac{1}{2} \delta^2 F_w^2 (1 - \cos 2\theta_I), \\ \widetilde{u}_I \widetilde{u}_R &= -K_R \delta^2 F_u^2 \cos \theta_I \cos \theta_R \\ &= -\frac{1}{2} K_R \delta^2 F_u^2 \left(\cos \left(\theta_I - \theta_R \right) + \cos \left(\theta_I + \theta_R \right) \right), \\ \widetilde{u}_R^2 &= K_R^2 \delta^2 F_u^2 \cos^2 \theta_I = \frac{1}{2} K_R^2 \delta^2 F_u^2 (1 + \cos 2\theta_R), \\ \widetilde{u}_I \widetilde{w}_R &= K_R \delta^2 F_u F_w \cos \theta_I \sin \theta_R \\ &= -\frac{1}{2} K_R \delta^2 F_u F_w \left(-\sin \left(\theta_I - \theta_R \right) + \sin \left(\theta_I + \theta_R \right) \right), \\ \widetilde{w}_I \widetilde{u}_R &= -K_R \delta^2 F_u F_w \sin \theta_I \cos \theta_R \\ &= -\frac{1}{2} K_R \delta^2 F_u F_w \left(\sin \left(\theta_I - \theta_R \right) + \sin \left(\theta_I + \theta_R \right) \right), \\ \widetilde{u}_R \widetilde{w}_R &= K_R^2 \delta^2 F_u F_w \sin \theta_R \cos \theta_R = \frac{1}{2} K_R^2 \delta^2 F_u F_w \sin 2\theta_R, \\ \widetilde{w}_I \widetilde{w}_R &= K_R \delta^2 F_w^2 \sin \theta_I \sin \theta_R = \frac{1}{2} K_R \delta^2 F_w^2 \left(\cos \left(\theta_I - \theta_R \right) - \cos \left(\theta_I + \theta_R \right) \right), \\ \widetilde{w}_R^2 &= K_R^2 \delta^2 F_w^2 \sin^2 \theta_R = \frac{1}{2} K_R^2 \delta^2 F_w^2 (1 - \cos 2\theta_R). \end{aligned} \tag{34}$$

The following step is to report all the components of the mean wave Reynolds tensors, both incident and reflected, for the mean and periodic equations.

The mean incident $\bar{r}_{ij}^I$ and reflected $\bar{r}_{ij}^R$ components stem from (33):

$$\begin{aligned} \bar{r}_{11}^I &= -\overline{\widetilde{u}_I^2} = -\frac{1}{2} \delta^2 F_u^2, \\ \bar{r}_{12}^I &= -\overline{\widetilde{u}_I \widetilde{w}_I} = 0, \\ \bar{r}_{22}^I &= -\overline{\widetilde{w}_I^2} = -\frac{1}{2} \delta^2 F_w^2, \\ \bar{r}_{11}^R &= -\left(\overline{2\widetilde{u}_I \widetilde{u}_R} + \overline{\widetilde{u}_R^2} \right) = K_R \delta^2 F_u^2 \left(\cos(\theta_I - \theta_R) - \frac{1}{2} K_R \right), \\ \bar{r}_{12}^R &= -\left(\overline{\widetilde{u}_I \widetilde{w}_R} + \overline{\widetilde{w}_I \widetilde{u}_R} + \overline{\widetilde{u}\widetilde{w}} \right) = K_R \delta^2 F_u F_w \sin(\theta_I - \theta_R), \\ \bar{r}_{22}^R &= -\left(\overline{2\widetilde{w}_I \widetilde{w}_R} + \overline{\widetilde{w}_R^2} \right) = -K_R \delta^2 F_w^2 \left(\cos(\theta_I - \theta_R) + \frac{1}{2} K_R \right). \end{aligned} \tag{35}$$

The periodic components of the incident $(\widetilde{r}_{ij}^I)$ and of the reflection-induced $(\widetilde{r}_{ij}^R)$ wave Reynolds tensors are derived from (34):

$$\begin{aligned} \widetilde{r}_{11}^I &= -\left(\widetilde{u}_I^2 + \bar{r}_{11}^I \right) = -\frac{1}{2} \delta^2 F_u^2 \cos 2\theta_I, \\ \widetilde{r}_{12}^I &= -\left(\widetilde{u}_I \widetilde{w}_I + \bar{r}_{12}^I \right) = \frac{1}{2} \delta^2 F_u F_w \sin 2\theta_I, \\ \widetilde{r}_{22}^I &= -\left(\widetilde{w}_I^2 + \bar{r}_{22}^I \right) = \frac{1}{2} \delta^2 F_w^2 \cos 2\theta_I, \\ \widetilde{r}_{11}^R &= -\left(2\widetilde{u}_I \widetilde{u}_R + \widetilde{u}_R^2 + \bar{r}_{11}^R \right) = K_R \delta^2 F_u^2 \left(\cos(\theta_I + \theta_R) - \frac{1}{2} K_R \cos 2\theta_R \right), \\ \widetilde{r}_{12}^R &= -\left(\widetilde{u}_I \widetilde{w}_R + \widetilde{w}_I \widetilde{u}_R + \widetilde{u}_R \widetilde{w}_R + \bar{r}_{12}^R \right) = -\frac{1}{2} K_R^2 \delta^2 F_u F_w \sin 2\theta_R, \\ \widetilde{r}_{22}^R &= -\left(2\widetilde{w}_I \widetilde{w}_R + \widetilde{w}_R^2 + \bar{r}_{22}^R \right) = K_R \delta^2 F_w^2 \left(\cos(\theta_I + \theta_R) + \frac{1}{2} K_R \cos 2\theta_R \right). \end{aligned} \tag{36}$$

Finally, we remind that $r_{ij} = r_{ji}$ for $i \neq j$.

References

Addona, F., Chiapponi, L., 2023. Velocity and stresses of partially-reflected water waves in the presence of opposing wind. Coast. Eng. 183, 104310.
Addona, F., Chiapponi, L., Clavero, M., Longo, S., 2024. Wind waves and swell interaction. Coast. Eng. submitted for publication.
Addona, F., Chiapponi, L., Clavero, M., Losada, M.A., Longo, S., 2020. On the interaction between partially-reflected waves and an opposing wind. Coast. Eng. 162, 103774.

Addona, F., Lira-Loarca, A., Chiapponi, L., Losada, M.A., Longo, S., 2018. The Reynolds wave shear stress in partially reflected waves. Coast. Eng. 138, 220–226.

Alves, J.H.G., Banner, M.L., Young, I.R., 2003. Revisiting the Pierson–Moskowitz asymptotic limits for fully developed wind waves. J. Phys. Oceanogr. 33 (7), 1301–1323.

Baquerizo, A., Losada, M.A., Smith, J.M., Kobayashi, N., 1997. Cross-shore variation of wave reflection from beaches. J. Waterw. Port Coast. Ocean Eng. 123 (5), 274–279.

Belcher, S.E., Harris, J.A., Street, R.L., 1994. Linear dynamics of wind waves in coupled turbulent air—water flow. Part 1. Theory. J. Fluid Mech. 271, 119–151.

Belcher, S., Hunt, J., 1993. Turbulent shear flow over slowly moving waves. J. Fluid Mech. 251, 109–148.

Benilov, A.Y., Filyushkin, B., 1970. Application of methods of linear filtration to an analysis of fluctuations in the surface layer of the sea. Izv., Acad. Sci., USSR, Atmos. Oceanic Phys. 68, 810–819.

Buckley, M.P., Veron, F., 2016. Structure of the airflow above surface waves. J. Phys. Oceanogr. 46 (5), 1377–1397.

Cao, T., Deng, B.-Q., Shen, L., 2020. A simulation-based mechanistic study of turbulent wind blowing over opposing water waves. J. Fluid Mech. 901.

Chen, G., Belcher, S.E., 2000. Effects of long waves on wind-generated waves. J. Phys. Oceanogr. 30 (9), 2246–2256.

Chen, X., Hara, T., Ginis, I., 2020. Impact of shoaling ocean surface waves on wind stress and drag coefficient in coastal waters: 1. Uniform wind. J. Geophys. Res.: Oceans 125 (7), e2020JC016222.

Cheung, T., Street, R., 1988. The turbulent layer in the water at an air—water interface. J. Fluid Mech. 194, 133–151.

Clavero, M., Longo, S., Chiapponi, L., Losada, M.A., 2016. 3D flow measurements in regular breaking waves past a fixed submerged bar on an impermeable plane slope. J. Fluid Mech. 802, 490–527.

De Vriend, H., Kitou, N., 1991. Incorporation of wave effects in a 3D hydrostatic mean current model. In: Coastal Engineering 1990. Elsevier, pp. 1005–1018.

Deigaard, R., Fredsøe, J., 1989. Shear stress distribution in dissipative water waves. Coast. Eng. 13 (4), 357–378.

Donelan, M., Anctil, F., Doering, J., 1992. A simple method for calculating the velocity field beneath irregular waves. Coast. Eng. 16 (4), 399–424.

Donelan, M.A., Drennan, W.M., Katsaros, K.B., 1997. The air–sea momentum flux in conditions of wind sea and swell. J. Phys. Oceanogr. 27 (10), 2087–2099.

Einaudi, F., Finnigan, J., 1981. The interaction between an internal gravity wave and the planetary boundary layer. Part I: The linear analysis. Q. J. R. Meteorol. Soc. 107 (454), 793–806.

Elgar, S., Herbers, T., Guza, R., 1994. Reflection of ocean surface gravity waves from a natural beach. J. Phys. Oceanogr. 24 (7), 1503–1511.

Feddersen, F., Veron, F., 2005. Wind effects on shoaling wave shape. J. Phys. Oceanogr. 35 (7), 1223–1228.

Garrett, C., Smith, J., 1976. On the interaction between long and short surface waves. J. Phys. Oceanogr. 6 (6), 925–930.

Grare, L., Peirson, W.L., Branger, H., Walker, J.W., Giovanangeli, J.P., Makin, V., 2013. Growth and dissipation of wind-forced, deep-water waves. J. Fluid Mech. 722, 5–50.

Hasselmann, K., 1971. On the mass and momentum transfer between short gravity waves and larger-scale motions. J. Fluid Mech. 50 (1), 189–205.

Hatori, M., Tokuda, M., Toba, Y., 1981. Experimental study on strong interaction between regular waves and wind waves—I. J. Oceanogr. Soc. Japan 37, 111–119.

Hsu, C.T., Hsu, E.Y., 1983. On the structure of turbulent flow over a progressive water wave: theory and experiment in a transformed wave-following coordinate system. Part 2. J. Fluid Mech. 131, 123–153.

Hussain, A., Reynolds, W., 1970. The mechanics of an organized wave in turbulent shear flow. J. Fluid Mech. 41 (2), 241–258.

Longuet-Higgins, M., 1969. A nonlinear mechanism for the generation of sea waves. Proc. R. Soc. A 311, 371–389.

Longuet-Higgins, M.S., Stewart, R.W., 1960. Changes in the form of short gravity waves on long waves and tidal currents. J. Fluid Mech. 8 (4), 565–583.

Lykke-Andersen, T., Clavero, M., Frigaard, P., M., L., Puyol, J.I., 2016. A new active absorption system and its performance to linear and non-linear waves. Coast. Eng. 114, 47–60.

Makin, V.K., Branger, H., Peirson, W.L., Giovanangeli, J.P., 2007. Stress above wind-plus-paddle waves: Modeling of a laboratory experiment. J. Phys. Oceanogr. 37 (12), 2824–2837.

Mansard, E.P.D., Funke, E.R., 1980. The measurement of incident and reflected spectra using a least squares method. In: Proc. 17th Coastal Engrg. Conf., vol. 1, American Society of Civil Engineers, pp. 154–172.

Miles, J.W., 1957. On the generation of surface waves by shear flows. J. Fluid Mech. 3 (2), 185–204.

Mitsuyasu, H., Honda, T., 1982. Wind-induced growth of water waves. J. Fluid Mech. 123, 425–442.

Olfateh, M., Ware, P., Callaghan, D.P., Nielsen, P., Baldock, T.E., 2017. Momentum transfer under laboratory wind waves. Coast. Eng. 121, 255–264.

Peirson, W.L., Garcia, A.W., Pells, S.E., 2003. Water wave attenuation due to opposing wind. J. Fluid Mech. 487, 345–365.

Phillips, O.M., 1957. On the generation of waves by turbulent wind. J. Fluid Mech. 2 (5), 417–445.

Phillips, O.M., 1963. On the attenuation of long gravity waves by short breaking waves. J. Fluid Mech. 16 (3), 321–332.

Pierson, Jr., W.J., Moskowitz, L., 1964. A proposed spectral form for fully developed wind seas based on the similarity theory of SA Kitaigorodskii. J. Geophys. Res. 69 (24), 5181–5190.

Rivero, F.J., Arcilla, A.S., 1995. On the vertical distribution of $\langle \tilde{u}\tilde{v} \rangle$. Coast. Eng. 25 (3–4), 137–152.

Semedo, A., Sušelj, K., Rutgersson, A., Sterl, A., 2011. A global view on the wind sea and swell climate and variability from ERA-40. J. Clim. 24 (5), 1461–1479.

Shabani, B., Nielsen, P., Baldock, T., 2014. Direct measurements of wind stress over the surf zone. J. Geophys. Res.: Oceans 119 (5), 2949–2973.

Smith, S.D., Anderson, R.J., Oost, W.A., Kraan, C., Maat, N., De Cosmo, J., Katsaros, K.B., Davidson, K.L., Bumke, K., Hasse, L., et al., 1992. Sea surface wind stress and drag coefficients: The HEXOS results. Boundary-Layer Meteorol. 60, 109–142.

Sullivan, P.P., McWilliams, J.C., 2010. Dynamics of winds and currents coupled to surface waves. Annu. Rev. Fluid Mech. 42.

Thais, L., Magnaudet, J., 1996. Turbulent structure beneath surface gravity waves sheared by the wind. J. Fluid Mech. 328, 313–344.

Villefer, A., Benoit, M., Violeau, D., Luneau, C., Branger, H., 2021. Influence of following, regular, and irregular long waves on wind-wave growth with fetch: An experimental study. J. Phys. Oceanogr. 51 (11), 3435–3448.